

Cite this: *RSC Adv.*, 2015, 5, 21090

Effect of pore geometries on the catalytic properties of NiO–Al₂O₃ catalysts in CO₂ reforming of methane

Xin Huang,^{ab} Nannan Sun,^{*c} Guangxin Xue,^{ab} Changzhen Wang,^d Haijuan Zhan,^{ab} Ning Zhao,^{ae} Fukui Xiao,^{ae} Wei Wei^{*c} and Yuhan Sun^c

Mesoporous NiO–Al₂O₃ catalysts were prepared by an evaporation-induced self-assembly (EISA) method, during which the amount of HNO₃ added in the precursor solution was varied. Characterization results indicated that the phase structure, component interaction and surface chemistry are fairly similar for all the samples, while the dispersion and textural properties, which are determined by the structure of the micelles and reaction rate of hydrolysis during the EISA process, changed significantly, thus leading to considerably different catalytic performance in CO₂ reforming of methane (CRM). The well-known trend that carbon formation rate decreases with the decrease of Ni particle size was observed in the current NA-Hx samples, however, it is very interesting that the disordered slit-like pores endowed the NA-H32 sample with a better capability to inhibit carbon formation as it showed substantially fewer carbon deposits as compared with NA-H16 (ordered cylindrical pore), despite the fact that the Ni particles in these samples are of similar size. In summary, the excellent performance of the NA-H32 catalyst in comparison to other non-promoted NiO–Al₂O₃ catalysts holds promise for using this cost-effective system in practical CRM applications.

Received 13th December 2014

Accepted 16th February 2015

DOI: 10.1039/c4ra16313c

www.rsc.org/advances

1. Introduction

In recent years, chemical conversion of CH₄ is drawing re-newed interest owing to the demand for low carbon resources and sustainable development. Furthermore, it is believed that the successful exploitation and recovery of shale gas in North America will further stimulate the use of CH₄ as a chemical feedstock in the near future.^{1,2} At the same time, huge amounts of CO₂ emitted by anthropogenic activities represent another concern that is closely related to the energy and environmental sectors of human society, and thus catalytic conversion of CO₂ to value-added products has been recognized as a potential solution for CO₂ reduction.^{3–7}

CO₂ reforming of methane (CRM), also known as dry reforming, has been well demonstrated to be a reaction that has economic plus environmental dual-benefits, namely the process converts CO₂ and CH₄ (which are the two major contributors to

the greenhouse effect) simultaneously, and produces syngas, which can be used for the synthesis of high quality fuels and other downstream chemicals.^{8–10} Unfortunately, cost- and performance-efficient catalysts have still not yet been accessed for practical deployment of the process.

Generally, active catalysts for the CRM reaction include Ni, Co, Fe, Ru, Pd and Pt, among which noble metals possessed excellent performance, but their limited availability makes them almost inhibitive for any industrial CRM applications.^{11–13} In this regards, Ni-based catalysts are more promising owing to their low cost. The activity of Ni-based catalysts can be effectively enhanced to achieve similar level of noble metals as long as the structure of the catalysts can be properly designed and fulfilled by a variety of preparation protocols.^{14,15} However, most of the Ni-based catalysts suffered from sintering and/or formation of inactive carbon residuals during CRM, which further deactivated the catalyst by either coverage of the active sites or decay of the catalysts structure.^{8–10,15}

Extensive researches have been carried out in order to maximize the advantages of the Ni-based catalysts without compromise to much on their stability, and a common conclusion from these works is that smaller Ni particles have a better capability to inhibit the formation of carbon.^{16–18} However, since CRM is normally performed at temperatures higher than 700 °C as the reaction is highly endothermic, it is not so straightforward to keep the metallic Ni sites from crystalline growth. To circumvent this, several strategies were

^aState Key Laboratory of Coal Conversion, Institute of Coal Chemistry, Chinese Academy of Sciences, Taiyuan 030001, China

^bUniversity of Chinese Academy of Sciences, Beijing 100049, China

^cCAS Key Laboratory of Low-Carbon Conversion Science and Engineering, Shanghai Advanced Research Institute, Chinese Academy of Sciences, Shanghai, 201210, China. E-mail: sunnn@sari.ac.cn; weiwei@sari.ac.cn

^dEngineering Research Center of Ministry of Education for Fine Chemicals, Shanxi University, Taiyuan 030006, China

^eNational Engineering Research Center for Coal-based Synthesis, Institute of Coal Chemistry, Chinese Academy of Sciences, Taiyuan 030001, China

developed, for example, Hu and co-workers contributed a series of papers on using NiO–MgO solid solution to catalyze CRM, since the Ni species in the system interact strongly with the support, sintering could be avoided effectively.^{18–21} Core-shell structured catalysts were also reported for CRM, where nano-sized Ni particles were maintained during reaction led to negligible carbon deposition.^{22,23} Another approach for preparing catalyst with improved thermal stability is to mimic naturally occurred mineral structure, such as perovskite.^{24–26} Recently, it was demonstrated that catalysts with ordered mesoporous structure showed promising performance in CRM.^{27–29} For example, Chou prepared ordered mesoporous NiO–CaO–Al₂O₃ catalysts, which exhibited excellent catalytic activities and stabilities in CRM.³⁰ Similarly, in Wang's work, it was reported that agglomeration of Ni particles was observed for Ni-impregnated NiCeAl catalyst, which accelerated the rate of carbon deposition, while on the ordered mesoporous catalyst, this was effectively inhibited leading to a high performing catalyst.³¹ However, since the catalysts in these works differ significantly in chemical compositions, a systematic and exclusive clarification and discussion on how different dispersive and textual properties can affect the catalytic properties are yet to be reported.

In the present paper, a NiO–Al₂O₃ system was selected as modal materials due to its simplicity, samples with different pore geometries was prepared by altering the structure of template micelle during the evaporation-induced self-assembly (EISA) process, the strategy led to the preparation of the NiO–Al₂O₃ catalysts with varying porous structure while keep other properties almost identical, which allowed us to individually analyse how the catalytic properties of the catalysts can be influenced by the dispersive and textual properties based on systematic characterizations of the fresh and used catalysts.

2. Experimental

2.1. Catalyst preparation

The mesoporous NiO–Al₂O₃ catalysts were prepared *via* one-pot EISA process following similar method reported by Yuan.³²

Typically, 1.0 g of Pluronic P123 (EO20PO70EO20, Sigma-Aldrich) was dissolved in 20 mL of anhydrous ethanol (J&K scientific Ltd.) at room temperature with vigorous stirring for 2 h, followed by addition of *x* mL of 67 wt% nitric acid (*x* = 0.4, 0.8, 1.6 and 3.2) and stirred for another 2 h. Then 9.5 mmol of aluminum iso-propoxide (98+%, Sigma-Aldrich) and 0.5 mmol nickel nitrate hexahydrate (AR, Sigma-Aldrich) were added into the above solution, the obtained precursor solution was covered with a PE film, stirred for *ca.* 5 h at room temperature, and then put into a drying oven pre-heated at 60 °C to slowly evaporate the solvent. After 48 h, the solution became a light-green dried gel, which was submitted to calcination in air by slowly increasing temperature with a ramping rate of 1 °C min^{−1} from room temperature to 800 °C and maintained at the final temperature for 5 h. The as-prepared mesoporous catalysts were then crushed and sieved, pellets of 20–40 meshes were collected and used in the CRM reaction. The mesoporous catalysts were denoted as NA-H*x* (*x* = 4, 8, 16 and 32, indicating the amounts

of HNO₃ added in the precursor solution are 0.4, 0.8, 1.6 and 3.2 mL, respectively) in the following text. According to elementary analysis using a Thermo iCAP6300 instrument, the Ni contents in all the prepared catalysts are around 5 wt% (4.96, 5.10, 5.01 and 5.26% for NA-H4, NA-H8, NA-H16 and NA-H32, respectively).

2.2. Catalyst characterization

Low temperature N₂ physisorption was carried out using a Micromeritics ASAP-2000 instrument. Prior to any tests, the catalysts were degassed at 200 °C overnight. Surface areas and the pore distribution were calculated using the Brunauer–Emmett–Teller (BET) and Barrett–Joyner–Halenda (BJH) method, respectively.

X-ray diffraction (XRD) patterns were recorded on a Bruker D8-advance diffractometer with Cu K α radiation (0.15418 nm) at room temperature from 10° to 80° (wide-angle) and 0.5° to 5° (small-angle). Measurements were conducted using a voltage of 40 kV, step size of 0.02° and current setting of 40 mA.

Transmission electron microscopy (TEM) images and energy-dispersive X-ray spectroscopy (EDX) measurements were carried out on a JEOL JEM-2100F under a working voltage of 200 kV.

H₂-temperature program reduction (H₂-TPR) was performed in a home-made apparatus. 50 mg catalyst was loaded and heated in an U-tube quartz reactor under Ar flow from room temperature to 500 °C to remove any physically adsorbed CO₂ and moisture, the temperature was then cooled down to room temperature and a 5 vol% H₂–Ar mixture was fed with a flow rate of 50 mL min^{−1}. The reduction process was started from room temperature to 1000 °C at a heating rate of 10 °C min^{−1}, a TCD was used to detect the consumption of H₂.

X-ray photoelectron spectroscopy (XPS) measurements were performed by a Kratos XSAM800 spectrometer with Al K α radiation (12 kV \times 15 mA, $h\nu$ = 1486.6 eV) under ultrahigh vacuum (10^{−7} Pa). The binding energies were calibrated internally by adventitious carbon deposit C (1s) with *E*_b = 284.6 eV (accuracy within \pm 0.1 eV).

TGA of the used catalysts were performed by using a Rigaku TG instrument from room temperature to 1000 °C with the rate of 10 °C min^{−1} under an air atmosphere (30 mL min^{−1}).

2.3. Catalyst evaluation

CRM was performed in a vertical quartz tube fixed-bed flow reactor (i.d. 6 mm) at atmospheric pressure, 700 °C, and a gas hourly space velocity (GHSV) of 48 L g^{−1} h^{−1} (CH₄ : CO₂ = 1). Typically, 100 mg of catalyst diluted with 300 mg of quartz sand was loaded into the quartz tube and supported by quartz wool. Prior to reaction, the catalyst was reduced at 800 °C with a 25 vol% H₂–N₂ mixture (80 mL min^{−1}) for 2 h. Before introducing the reaction gases, the catalyst bed was purged with N₂ (60 mL min^{−1}) until the reaction temperature was achieved and stabilized. The effluent gases were cooled in a cooling trap to remove any by-produced water, and gaseous products from the reactor were analysed by an online gas chromatograph with a TDX-01 column and a TCD detector.

3. Results and discussion

3.1. NA-Hx catalysts with similar phase structure, Ni–Al interactions and surface chemistry

3.1.1. Wide-angle XRD. Wide-angle XRD (WXR) was used to analyse the phase structure of the NA-Hx catalysts and the results are showed in Fig. 1. Three peaks located at *ca.* 36.9, 45.7, and 66.6° emerged in all the spectrums, which can be related to either γ - Al_2O_3 (JCPDS card no. 10-0425) or NiAl_2O_4 spinel (JCPDS card no. 10-0339) as the diffraction peaks of these phases are overlapped. According to previous reports, the NiAl_2O_4 spinel phase has a higher possibility to exist owing to the high calcination temperature used in the present study.^{33–36} Anyway, the low intensity of the peaks indicates that the NiAl_2O_4 phase in all the samples occurred to be highly amorphous. On the other hand, no diffraction peaks of nickel oxide can be observed, indicating a highly dispersed state of Ni-bearing species thanks to the mesoporous skeleton of the catalysts (see below).

3.1.2. H_2 -TPR. Reducibility of the catalysts and thus the interactions between the Ni- and Al-containing species were characterized by H_2 -TPR as showed in Fig. 2. For all the samples, only a peak at *ca.* 840–880 °C can be observed, which is indicative for the occurrence of strong interactions between Ni- and Al-containing species. The results are expectable since the formation of NiAl_2O_4 spinel has been confirmed by the WXR analysis (Section 3.1.1). No H_2 -consumption was observed at temperatures low than 400 °C, suggesting that the amount of free NiO with little NiO– Al_2O_3 interactions is negligible. The similar patterns observed from the curves in Fig. 2 evidenced the chemical properties of all the samples are literally identical, most probably due to the similar chemical processes (sol-formation, gelation, *etc.*) during the preparation of the samples.

3.1.3. XPS. The surface chemistry of the samples was further characterized by means of XPS, the obtained Ni2p spectres are showed in Fig. 3. For all the samples, a peak centred around 856.2 eV can be seen together with a shake-up satellite peak at 862.0 eV. These are the typical signals for the NiAl_2O_4 spinel according to Ng and others.^{37–39} Since the Ni2p peak for pure NiO is located at 853.6 eV,³⁹ therefore it is obvious that most of the Ni species in the as-prepared catalysts exists in the

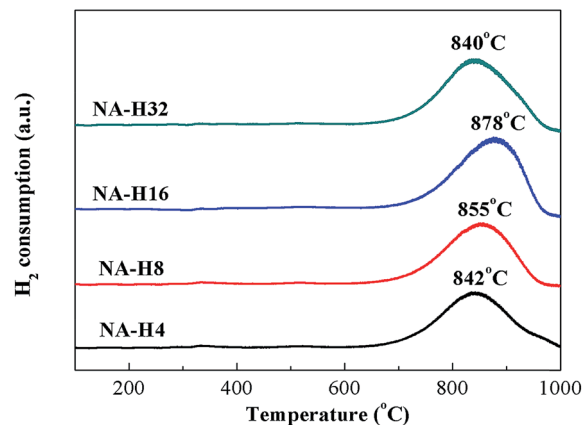


Fig. 2 H_2 -TPR profiles of the NA-Hx catalysts.

form of NiAl_2O_4 spinel, this conclusion is in accordance with those found by WXR and H_2 -TPR, which verifies again that the chemical properties among the NA-Hx catalysts are fairly similar.

3.2. Textural properties and morphologies of the NA-Hx catalysts

3.2.1. N_2 adsorption–desorption. The specific surface area, pore volume and average pore diameter of the NA-Hx catalysts were measured by low temperature N_2 physisorption, and the results are summarized in Table 1. Substantially developed porous structures are observed for all the catalysts although they were submitted to high temperature calcination (800 °C). With the increase of HNO_3 used during the preparation, both the BET surface area and pore volume increased and reached a maximum for the NA-H8 catalyst ($312 \text{ m}^2 \text{ g}^{-1}$ and $0.55 \text{ cm}^3 \text{ g}^{-1}$, respectively), further increasing the amount of HNO_3 led to decreased surface areas and pore volumes.

The nitrogen adsorption and desorption isotherms of the fresh NA-Hx catalysts are showed in Fig. 4(a). According to the

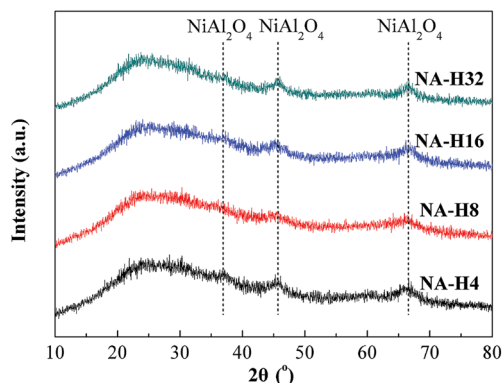


Fig. 1 Wide-angle XRD of the calcined NA-Hx catalysts.

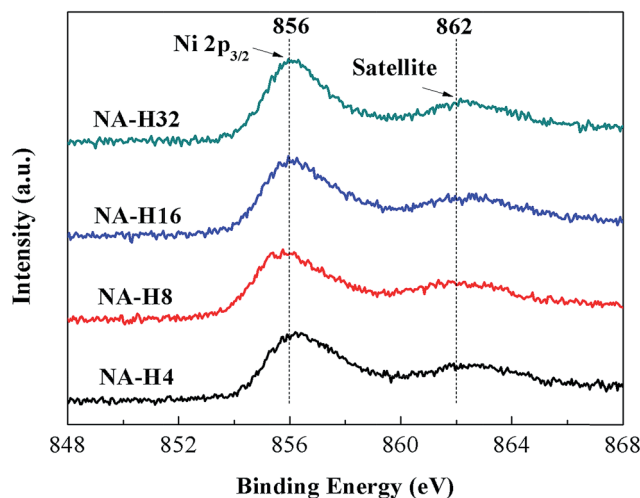


Fig. 3 XPS profiles of the calcined NA-Hx catalysts.

Table 1 Textural properties of the calcined and used^a NA-Hx catalysts

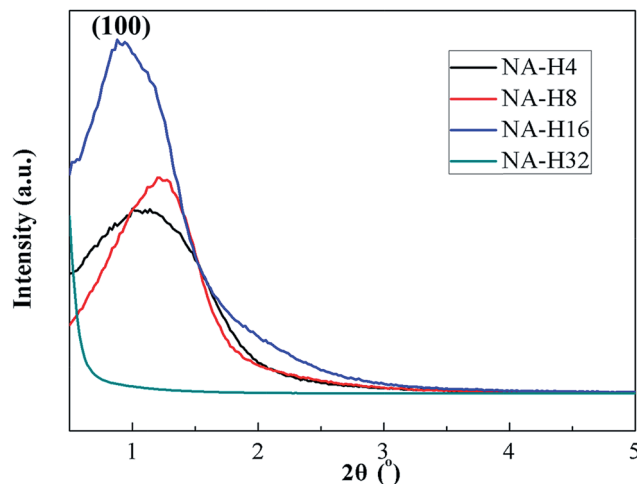
Catalysts	Specific surface area (m ² g ⁻¹)		Pore volume (cm ³ g ⁻¹)		Average pore diameter (nm)	
	Calcined	Used	Calcined	Used	Calcined	Used
NA-H4	259	221	0.34	0.30	3.5	4.0
NA-H8	312	271	0.55	0.47	4.5	4.8
NA-H16	247	176	0.51	0.39	5.5	6.7
NA-H32	153	150	0.37	0.35	6.6	7.1

^a The used catalysts were the catalysts tested under the following conditions for 50 h: 700 °C, 1 atm, CH₄ : CO₂ = 1 and GHSV = 48 L g⁻¹ h⁻¹.

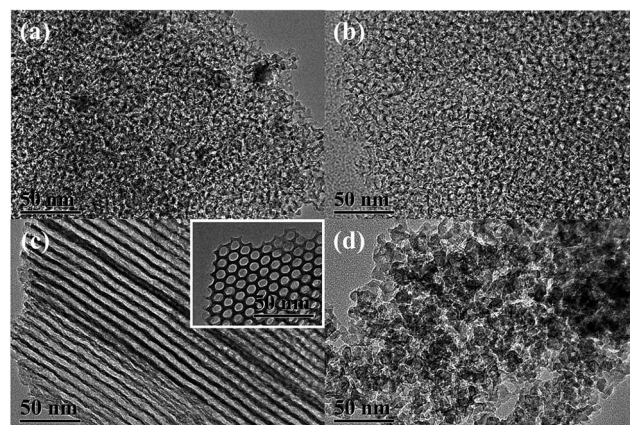
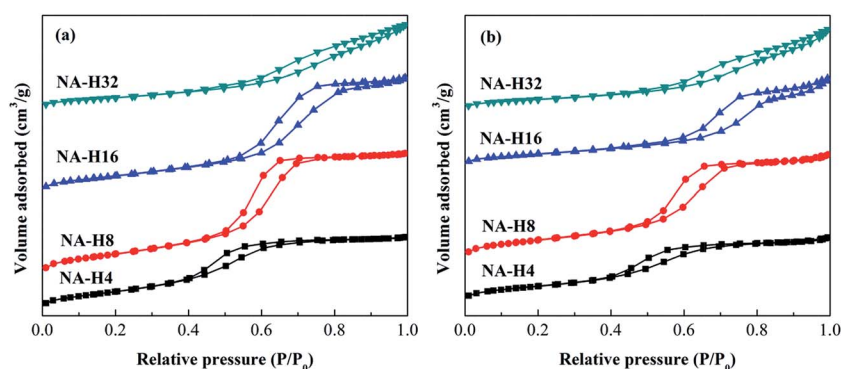
IUPAC classification,⁴⁰ all catalysts exhibited typical type IV isotherms with H1 shaped hysteresis loops between $P/P_0 = 0.5$ – 0.8 except for the NA-H32 catalyst, indicating that the structures of the samples possessed facile pore connectivity and relatively high uniformity. In the case of the NA-H32 catalyst however, a type IV isotherm with a H3 shaped hysteresis loops was obtained, suggesting that the NA-H32 catalyst is characterized by slit-like pores formed by the accumulation of plate-like aggregated particles.⁴¹

3.2.2. Small-angle XRD. Small-angle XRD (SAXRD) was performed to characterize the porous uniformity of the NA-Hx catalysts as showed in Fig. 5. Apart from the NA-H32 catalyst, all patterns presented a strong peak at *ca.* 1°, which is attributable to the short-range structural ordering with uniform pore sizes of these samples, among them, NA-H16 catalyst exhibited the strongest peak due to the highest pore uniformity. By contrast, no diffraction peaks can be observed from the patterns for the NA-H32 catalyst, confirming the disordered slit-pore structure as discussed in Section 3.2.1.

3.2.3. TEM. A direct observation of the structural properties of the NA-Hx samples was made by means of TEM, and the obtained TEM pictures are showed in Fig. 6. The samples of NA-H4 (Fig. 6(a)) and NA-H8 (Fig. 6(b)) showed a sponge-like structure, and evenly distributed mesopores with quasi-identical pore diameter can be observed, which might be responsible to the broad SAXRD peaks as showed in Fig. 5. For the sample NA-H16 however, highly ordered arrays of

**Fig. 5** Small-angle XRD of as-synthesized NA-Hx catalysts calcined at 800 °C.

cylindrical pores along [110] direction and hexagonal arrangement of pores along [001] direction were obtained (Fig. 6(c)). Further increasing the HNO₃ amount during preparation, a

**Fig. 6** TEM images of the calcined (a) NA-H4, (b) NA-H8, (c) NA-H16 and (d) NA-H32 catalysts.**Fig. 4** Nitrogen adsorption–desorption isotherms of the (a) calcined and (b) used NA-Hx catalysts.

structure composed with the disordered aggregates can be seen for the sample NA-H32. Combined with BET and SXRD analysis, it is reasonable to assume that disordered slit-like pores were formed for the sample NA-H32. Nevertheless, it is difficult to locate any Ni species from the meso-structures for all the catalysts, however, EDX measurements indicated exclusive peaks for Ni, O and Al (not shown), implying that Ni was successfully introduced, these results verifies again that during the EISA process and subsequent calcination, the precursors converted into a NiO–Al₂O₃ mixed-oxide, most likely in the form of NiAl₂O₄ spinel, and thus evenly distributed morphologies are observed.

The TEM images of the NA-Hx samples after reduction are presented in Fig. 7, it can be seen that despite the features of the meso-structures were almost remain unchanged (*e.g.* sponge-like and well-ordered frameworks for NA-H8 and NA-H16, respectively), Ni particles emerged for all the catalysts owing to the partial reduction of Ni species in the NiAl₂O₄ spinel. It seems that the framework morphology of the samples had a significant influence on the obtained Ni particles, from the particle size distribution (inserts in Fig. 7), it can be found that with the increasing amount of HNO₃ used during preparation, the average size of the obtained Ni particles decreased from 17.2 nm for NA-H4 to 10.1 nm for NA-H32. More interestingly, the percentage of particles with sizes ± 1.5 nm to the peak value of the distribution curves (insert of Fig. 7) can be calculated to be 32.0, 42.3, 66.7 and 58.3% for NA-H4, NA-H8, NA-H16 and NA-H32, indicating that sample NA-H16 and NA-H32 showed a narrower particle size distribution as compared with those for NA-H4 and NA-H8. Furthermore, the average pore sizes were smaller than the Ni average sizes for all the NA-Hx catalysts, revealing that metallic Ni is embedded and anchored in the meso-structure of the catalysts during the one-pot EISA process, similar conclusion was also reported in the previous investigations.^{14,27,30,31,36}

Bearing the above characterization results in mind, it is necessary to have detailed summary and discussion on the effects of HNO₃ on the formation of different meso-structures of the current NA-Hx samples. It has been demonstrated by Yuan

et al. that during an EISA process, many factors such as acidity, proportions of precursors, volatilization of the solvents, amount of water and others will substantially influence the formation of the meso-structures.³² In the present study, different amount of HNO₃ was used when preparing the precursor solutions while all other factors/conditions were maintained constantly, since the NO₃[−] anion can hardly coordinate with Al³⁺ in aqueous environment, it is believable that the different meso-structures can be attributed exclusively to the difference in H⁺ and H₂O concentrations of the precursor solutions.

Basically, an important step during the hydrolysis of aluminum iso-propoxide is substitution of protonized iso-propoxy groups by a H₂O molecule, this is to say that in the process, H⁺ and H₂O act as catalyst and reactant, respectively. Based on this, it is expectable that the hydrolysis during the preparation of NA-H4 and NA-H8 was relatively slow, and thus there is a longer time for the diffusion and gathering of Ni²⁺ (similar to Ostwald ripening) before the gel framework became more rigid, so that larger Ni-bearing domains were formed which further led to the formation of larger Ni particles after reduction (Fig. 7(a) and (b)). On the other hand, Ni particles obtained on NA-H16 and NA-H32 were smaller since smaller Ni²⁺ ion clusters were “anchored” in the gel framework and lost their mobility when extra HNO₃ was used during the gelation as indicated in Fig. 7(c) and (d).

In fact, the role of H₂O during the gelation is more than a reactant. According to Soler-Illia *et al.*, H₂O will also affect the formation of micelles by folding the template molecule *via* enhancing the solubility difference between the PEO and PPO blocks in the template molecule, and the structure of the obtained micelles can thus been influenced significantly.⁴² When the H₂O content in the system is low, the template molecule is more likely to adopt a “vermicular” structure, and the gel particles are condensed along the “curling template chain” leading to the formation of the sponge-like mesoporous structure as observed in the sample NA-H4 and NA-H8 (Fig. 6(a) and (b)). The lack of long-range ordering of the meso-structures owing to the inadequate folding of the template was also reported previously.⁴³ With the increasing of H₂O content, formation of rod-like micelles and their subsequent assembly to highly ordered hexagonal liquid crystal phase can be achieved, and thus the resulted NA-H16 sample showed periodical arrays of mesopores (Fig. 6(c)). As for the sample NA-H32, the template molecule is over-folded causing the formation of ill-structured gels, making the final catalyst a disordered structure (Fig. 6(d)). Similar observations were also reported by Niesz *et al.*⁴⁴

3.3. Catalytic performance of the NA-Hx catalysts in CRM

Dry reforming was carried out over the NA-Hx catalysts at atmospheric pressure and 700 °C with a gas hourly space velocity of 48 L g^{−1} h^{−1} for 50 h and the obtained results are presented in Fig. 8 and Table 2. As can be seen, the performance of the catalysts in terms of activity and stability were improved substantially with the increase of the *x* value, namely higher amount of HNO₃ used in the preparation resulted in a higher

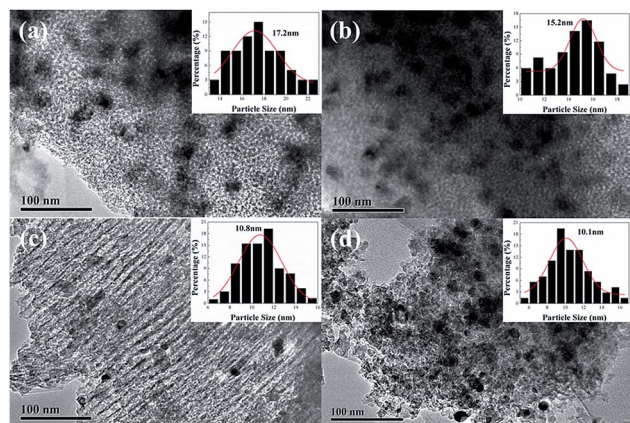


Fig. 7 TEM images and corresponding Ni particle size distributions for the reduced (a) NA-H4, (b) NA-H8, (c) NA-H16 and (d) NA-H32 catalysts.

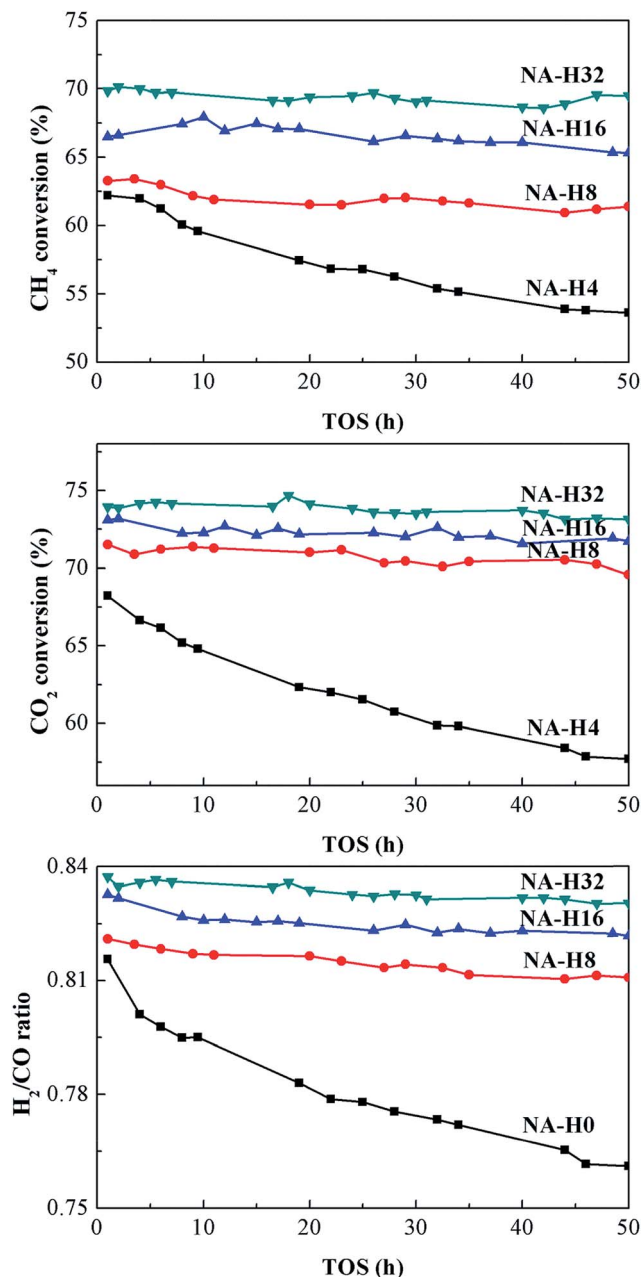


Fig. 8 Long-term stability tests over the NA-Hx catalysts for 50 h, reaction conditions: 700 °C, 1 atm, $\text{CH}_4 : \text{CO}_2 = 1$, $48 \text{ L g}^{-1} \text{ h}^{-1}$.

catalytic performance. For example the NA-H32 catalyst exhibited a CH_4 conversion of *ca.* 70%, which is close to the equilibrium conversion (73%, as calculated *via* HSC Chemistry

software, not shown here.) at the reaction conditions with negligible deactivation during 50 h reaction. In contrast, decay of CH_4 conversion can be observed over the samples with a smaller x value, especially for the NA-H4 sample, which showed an average deactivation rate of $0.1750\% \text{ h}^{-1}$ as compared with $0.0068\% \text{ h}^{-1}$ for the NA-H32 catalyst.

3.4. Characterization of the used catalysts

Since the phase structures and interactions between the components among the NA-Hx samples are fairly similar (Section 3.1), it is thus reasonable to attribute their different catalytic performance to the significantly varied dispersion and texture properties. In this section, the used catalysts were characterized and the results, together with those obtained earlier on the fresh catalyst, were used to clarify the key factors in determining the promising performance of the NA-H32 catalyst.

Fig. 9 shows the WXR patterns of the reduced and used catalysts. As presented in Fig. 9(a), there were no diffraction peaks of metallic Ni for the reduced NA-Hx catalysts, suggesting that metallic Ni is amorphous and/or highly dispersed over the catalysts. For the used catalysts, highly broadened curves similar to their reduced counterparts were obtained indicating that sintering of the mesoporous framework is negligible. In line with the results from Fig. 7, peaks corresponding to metallic Ni can be seen at *ca.* 44.5° and 51.8° owing to the partial reduction of the NiAl_2O_4 spinel, however, the intensity of the peaks are too low to determine the particle sizes. Compared with WXR patterns of the reduced NA-Hx catalysts, the diffraction peaks of the metallic Ni appeared for the used NA-Hx catalysts, suggesting that slightly sintering of Ni species occurred during the reforming reaction. This can be confirmed by TEM as showed Fig. 10, where Ni particles exist with average sizes ranging from 11.6 to 21.8 nm, slightly higher than those observed for the reduced catalysts (Fig. 7).

As has been well established in the open literatures, sintering of Ni particles represents an important factor leading to deactivation of reforming catalysts.^{9,10,17} In the present case however, the growth of Ni particles observed by TEM may not necessarily be accounted as “sintering” since the increasing of particle sizes is limited as compared with catalysts prepared by impregnation,^{45,46} and more importantly, it has been demonstrated^{54–56} that for catalysts prepared *via* one-step methods (such as co-precipitation or sol-gel), some nano-sized Ni domains are highly active and thus occurs to be the major

Table 2 Deactivation rate and carbon deposition of the used^a NA-Hx catalysts

Catalysts	Deactivation rate ^a ($\% \text{ h}^{-1}$)	Carbon deposition ($\text{g}_\text{C} \text{ g}_{\text{cat}}^{-1}$)	Average carbon deposition rate ($\text{mg}_\text{C} \text{ g}_{\text{cat}}^{-1} \text{ h}^{-1}$)
NA-H4	0.1750	0.500	10.00
NA-H8	0.0386	0.223	4.46
NA-H16	0.0238	0.188	3.76
NA-H32	0.0068	0.129	2.58

^a Deactivation rate = $(\text{CH}_4 \text{ conversion}_{1\text{h}} - \text{CH}_4 \text{ conversion}_{50\text{h}})/49$. Reforming reaction: 700 °C, 1 atm, $\text{CH}_4 : \text{CO}_2 = 1$, GHSV = $48 \text{ L g}^{-1} \text{ h}^{-1}$ and 50 h.

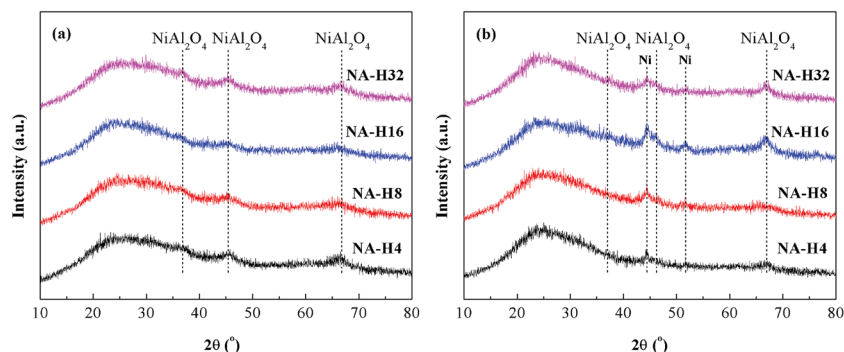


Fig. 9 Wide-angle XRD of the (a) reduced and (b) used NA-Hx catalysts.

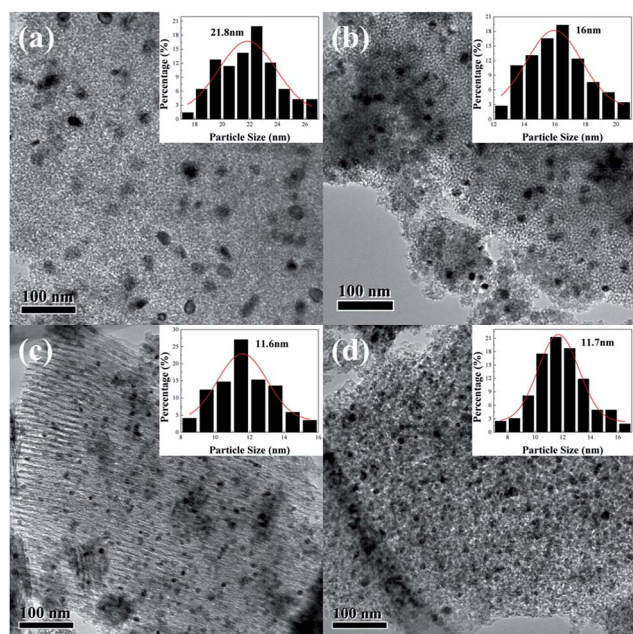


Fig. 10 TEM images and corresponding Ni particle size distributions for the used (a) NA-H4, (b) NA-H8, (c) NA-H16 and (d) NA-H32 catalysts.

catalytic sites rather than those larger ones as observed in Fig. 10.

In addition to sintering, carbon formation is another reason that may induce catalyst deactivation. To have a quantified measurement of the formed carbon on the used NA-Hx catalysts, TGA of the used catalysts was carried out in an air atmosphere as showed in Fig. 11. Based on the weight losing curves, amounts of carbon formation and their average formation rate could be calculated as listed in Table 2. It is obvious that the deactivation rate of the NA-Hx catalysts is in accordance with the average carbon formation rate, *e.g.* sample NA-H32 with the highest stability showed the lowest carbon formation rate of $2.58 \text{ mg}_c \text{ g}_{\text{cat}}^{-1} \text{ h}^{-1}$, this is strong evidence that deactivation of the catalysts can mainly be attributed to the formation of carbon species. Meanwhile, decreasing of textural properties can be observed for the used NA-H4, NA-H8 and NA-H16 owing to the blockage of the pores by the formed carbon (Fig. 4 and

Table 1). On the other hand, the BET surface area and pore volume for the used NA-H32 is almost the same as compared with fresh NA-H32 thanks to the lower amount of the formed carbon.

In addition, a general trend that can be summarized from Table 2 and Fig. 10 is that faster carbon formation is observed on catalysts with larger Ni particles as has already been reported extensively.^{16,47,48} For example, Tao *et al.* reported that a $\text{Ni-Ce}_{0.8}\text{Zr}_{0.2}\text{O}_2$ catalyst prepared by a sol-gel auto-combustion method showed enhanced stability owing to the smaller Ni crystalline size, while catalyst derived from co-precipitation (with larger Ni particles) suffered from higher amount of carbon deposition.⁵⁷ In the present case however, it is very interesting to have a comparison between the coking behaviour of NA-H16 and NA-H32, as indicated from Fig. 7, these samples exhibited similar Ni particle sizes, but the carbon formation rate varied significantly and thus leading to an obvious difference in terms of deactivation rate (Table 2). According to the above characterization of both the fresh and used NA-H16 and NA-H32, the major difference between these two samples is the pore geometry, namely NA-H16 featured highly ordered arrays of mesopores while NA-H32 is characterized by a disordered slit-like mesoporous structure, since all these features were retained in the used catalysts, it can be concluded that carbon formation

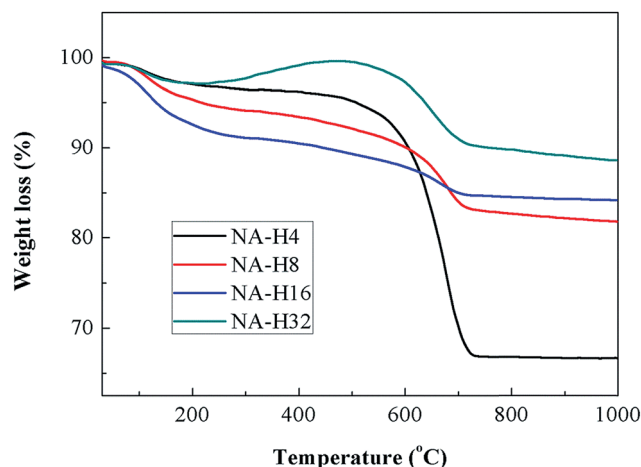


Fig. 11 TGA curves of 50 h stability tested catalysts.

on the NA-H32 was inhibited due to its unique disordered slit-like pores. One possible explanation to the observed effect of pore geometry on the carbon formation can be given based on similar assumptions reported by Bao and others,^{49–51} who demonstrated that due to the curvature of the walls of carbon nanotubes (CNTs), the π electrons may shift from the concave inner to the convex outer surface, leading to the formation of an electric potential difference. As for the current NA-H16 and NA-H32 samples, we believe that the difference in electric field owing to the surface curvature may not as obvious as in the CNTs owing to the lower conductivity, however, even minor localized distribution of electrons (negatively charged) will alter the chemical activity of oxygen-related sites (lattice oxygen atoms and/or oxygen vacancies), and thus the elimination of the formed carbon deposits can be influenced,^{52,53} we are currently carrying out detailed investigations on the reasoning of this observation.

Recently, several groups have reported that CRM catalysts with an ordered mesoporous structure showed important advantages on activity and stability over disordered ones.^{27–29} However, we showed here that in the EISA precursor solution, when the template molecule was over-folded and extra H^+ was introduced to accelerate the hydrolysis process, the obtained NA-H32 sample with a highly disordered structure overperformed the ordered mesoporous NA-H16. Moreover, non-promoted $NiO-Al_2O_3$ systems have rarely been reported to show a stable performance as was observed on the present NA-H32 sample, *e.g.* according to McFarlane and co-worker, substantial decay of H_2 production during CRM was observed on an impregnated Ni/Al_2O_3 catalyst,⁵⁸ therefore we believe that the current result is actually fairly encouraging, and holds the possibility of using the cheap and widely available $NiO-Al_2O_3$ based catalysts for practical reforming processes.

4. Conclusions

In summary, a series of $NiO-Al_2O_3$ catalysts were prepared and used as model catalysts in CO_2 reforming of methane. It was found that the dispersion of Ni-bearing species and pore geometry of the catalysts influenced significantly the catalytic behaviour, and the sample NA-H32 exhibited excellent activity and stability, the high amount of HNO_3 used for the preparation of this catalyst accelerated the hydrolysis of the precursors, therefore small Ni-bearing clusters had little chance to gather and grow into larger domains before the gel structure became rigid, leading to the formation of small Ni particles in the reduced catalyst. Furthermore, the high concentration of H_2O in the precursor solution enhanced the bending of the template molecule, making the final catalyst a disordered slit-like porous framework, this unique structure can not only stabilize the nano-sized Ni particles, but also renders the catalysts a high capability to avoid carbon formation. Consequently, the NA-H32 catalyst exhibited an excellent performance in CO_2 reforming of methane, which even outperformed sample NA-H16 with an ordered cylindrical mesopores, such a stable $NiO-Al_2O_3$ catalyst has rarely reported before, we believe the present findings are

important as they demonstrated the possibility of using the cost-effective $NiO-Al_2O_3$ system for practical CRM applications.

Acknowledgements

The authors wish to acknowledge the financial support from the National Natural Science Foundation of China (21203230), the National Basic Research Program of China (2011CB201405), the Key Science and Technology Program of Shanxi Province, China (MD2014-10).

Notes and references

- 1 J. J. Spivey and G. Hutchings, *Chem. Soc. Rev.*, 2014, **43**, 792.
- 2 H. F. Abbas and W. M. A. W. Daud, *Int. J. Hydrogen Energy*, 2010, **35**, 1160.
- 3 D. Pakhare and J. Spivey, *Chem. Soc. Rev.*, 2014, **43**, 7813.
- 4 M. Aresta and A. Dibenedetto, *Dalton Trans.*, 2007, 2975.
- 5 C. Song, *Catal. Today*, 2006, **115**, 2.
- 6 S. Perathoner and G. Centi, *ChemSusChem*, 2014, **7**, 1274.
- 7 J. Ma, N. Sun, X. Zhang, N. Zhao, F. Xiao, W. Wei and Y. Sun, *Catal. Today*, 2009, **148**, 221.
- 8 A. T. Ashcroft, A. K. Cheetham, M. L. H. Green and P. D. F. Vernon, *Nature*, 1991, **352**, 225.
- 9 Y. H. Hu and E. Ruckenstein, *Adv. Catal.*, 2004, **48**, 297.
- 10 M. C. J. Bradford and M. A. Vannice, *Catal. Rev.: Sci. Eng.*, 1999, **41**, 1.
- 11 J. Zhang, H. Wang and A. Dalai, *J. Catal.*, 2007, **249**, 300.
- 12 M. C. J. Bradford and M. A. Vannice, *J. Catal.*, 1998, **173**, 157.
- 13 J. R. Rostrup-Nielsen and J.-H. B. Hansen, *J. Catal.*, 1993, **144**, 38.
- 14 L. Xu, H. Song and L. Chou, *Catal. Sci. Technol.*, 2011, **1**, 1032.
- 15 N. Sun, X. Wen, F. Wang, W. Peng, N. Zhao, F. Xiao, W. Wei, Y. Sun and J. Kang, *Appl. Surf. Sci.*, 2011, **257**, 9169.
- 16 J. H. Kim, D. J. Suh, T. J. Park and K. L. Kim, *Appl. Catal., A*, 2000, **197**, 191.
- 17 Y. H. Hu, *Catal. Today*, 2009, **148**, 206.
- 18 Y. H. Hu and E. Ruckenstein, *Catal. Rev.: Sci. Eng.*, 2002, **44**, 423.
- 19 Y. H. Hu and E. Ruckenstein, *Catal. Lett.*, 1996, **36**, 145.
- 20 E. Ruckenstein and Y. H. Hu, *Appl. Catal., A*, 1997, **154**, 185.
- 21 Y. H. Hu and E. Ruckenstein, *Catal. Lett.*, 1997, **43**, 71.
- 22 Z. Li, L. Mo, Y. Kathiraser and S. Kawi, *ACS Catal.*, 2014, **4**, 1526.
- 23 T. Wu, W. Cai, P. Zhang, X. Song and L. Gao, *RSC Adv.*, 2013, **3**, 23976.
- 24 T. Odedairo, W. Zhou, J. Chen and Z. Zhu, *RSC Adv.*, 2014, **4**, 21306.
- 25 S. E. Evans, O. J. Good, J. Z. Staniforth, R. M. Ormerod and R. J. Darton, *RSC Adv.*, 2014, **4**, 30816.
- 26 G. S. Gallego, F. Mondragón, J. Barrault, J. M. Tatibouët and C. B. Dupeyrat, *Appl. Catal., A*, 2006, **311**, 164.
- 27 L. Xu, H. Song and L. Chou, *Appl. Catal., B*, 2011, **108–109**, 177.

- 28 N. Wang, Z. Xu, J. Deng, K. Shen, X. Yu, W. Qian, W. Chu and F. Wei, *ChemCatChem*, 2014, **6**, 1.
- 29 S. Zhang, S. Muratsugu, N. Ishiguro and M. Tada, *ACS Catal.*, 2013, **3**, 1855.
- 30 L. Xu, H. Song and L. Chou, *ACS Catal.*, 2012, **2**, 1331.
- 31 N. Wang, K. Shen, L. Huang, X. Yu, W. Qian and W. Chu, *ACS Catal.*, 2013, **3**, 1638.
- 32 Q. Yuan, A. X. Yin, C. Luo, L. D. Sun, Y. W. Zhang, W. T. Duan, H. C. Liu and C. H. Yan, *J. Am. Chem. Soc.*, 2008, **130**, 3465.
- 33 J. M. Rynkowski, T. Paryjczak and M. Lenik, *Appl. Catal., A*, 1993, **106**, 73.
- 34 N. Sahli, C. Petit, A. C. Roger, A. Kiennemann, S. Libs and M. M. Bettahar, *Catal. Today*, 2006, **113**, 187.
- 35 S. M. Morris, P. F. Fulvio and M. Jaroniec, *J. Am. Chem. Soc.*, 2008, **130**, 15210.
- 36 Q. Zhang, T. Wu, P. Zhang, R. Qi, R. Huang, X. Song and L. Gao, *RSC Adv.*, 2014, **4**, 51184.
- 37 K. T. Ng and D. M. Hercules, *J. Phys. Chem.*, 1976, **80**, 2094.
- 38 G. R. Gavalas, C. Phichitkul and G. E. Voecks, *J. Catal.*, 1984, **88**, 54.
- 39 Y. S. Oh, H. S. Roh, K. W. Jun and Y. S. Baek, *Int. J. Hydrogen Energy*, 2003, **28**, 1387.
- 40 K. S. W. Sing, D. H. Everett, R. A. W. Haul, L. Moscou, R. A. Pierotti, J. Rouquérol and T. Siemienińska, *Pure Appl. Chem.*, 1985, **57**, 603.
- 41 M. Kruk and M. Jaroniec, *Chem. Mater.*, 2001, **13**, 3169.
- 42 G. J. d. A. A. Soler-Illia and C. Sanchez, *New J. Chem.*, 2000, **24**, 493.
- 43 G. J. d. A. A. Soler-Illia, E. Scolan, A. Louis, P. A. Albouy and C. Sanchez, *New J. Chem.*, 2001, **25**, 156.
- 44 K. Niesz, P. Yang and G. A. Somorjai, *Chem. Commun.*, 2005, 1986.
- 45 C. Wang, N. Sun, N. Zhao, W. Wei, J. Zhang, T. Zhao, Y. Sun, C. Sun, H. Liu and C. E. Snape, *ChemCatChem*, 2014, **6**, 640.
- 46 C. Wang, N. Sun, M. Kang, X. Wen, N. Zhao, F. Xiao, W. Wei, T. Zhao and Y. Sun, *Catal. Sci. Technol.*, 2013, **3**, 2435.
- 47 V. C. H. Kroll, H. W. Swann and C. Mirodatos, *J. Catal.*, 1996, **161**, 409.
- 48 S. Tang, L. Ji, J. Lin, H. C. Zeng, K. L. Tan and K. Li, *J. Catal.*, 2000, **194**, 424.
- 49 W. Chen, Z. Fan, X. Pan and X. Bao, *J. Am. Chem. Soc.*, 2008, **130**, 9414.
- 50 A. Tavasoli, M. Trépanier, A. K. Dalai and N. Abatzoglou, *J. Chem. Eng. Data*, 2010, **55**, 2757.
- 51 X. Pan and X. Bao, *Acc. Chem. Res.*, 2011, **44**, 553.
- 52 M. García-Diéguez, I. S. Pieta, M. C. Herrera, M. A. Larrubia and L. J. Alemany, *J. Catal.*, 2010, **270**, 136.
- 53 W. Wang, S. M. Staggs-Williams, F. B. Noronha, L. V. Mattos and F. B. Passos, *Catal. Today*, 2004, **98**, 553.
- 54 R. Pereniguez, V. M. Gonzalez-delaCruz, A. Caballero and J. P. Holgado, *Appl. Catal., B*, 2012, **123**, 324.
- 55 M. Nurunnabi, Y. Mukainakano, S. Kado, B. Li, K. Kunimori, K. Suzuki, K. Fujimoto and K. Tomishige, *Appl. Catal., A*, 2006, **299**, 145.
- 56 M. Nurunnabi, K. Fujimoto, K. Suzuki, B. Li, S. Kado, K. Kunimori and K. Tomishige, *Catal. Commun.*, 2006, **7**, 73.
- 57 K. Tao, S. Zhou, Q. Zhang, C. Kong, Q. Ma, N. Tsubaki and L. Chen, *RSC Adv.*, 2013, **3**, 22285.
- 58 A. R. McFarlane, I. P. Silverwood, R. Warringham, E. L. Norris, R. M. Ormerod, C. D. Frost, S. F. Parker and D. Lennon, *RSC Adv.*, 2013, **3**, 16577.